# RSC Advances

This is an *Accepted Manuscript*, which has been through the Royal Society of Chemistry peer review process and has been accepted for publication.

*Accepted Manuscripts* are published online shortly after acceptance, before technical editing, formatting and proof reading. Using this free service, authors can make their results available to the community, in citable form, before we publish the edited article. This *Accepted Manuscript* will be replaced by the edited, formatted and paginated article as soon as this is available.

You can find more information about *Accepted Manuscripts* in the **Information for Authors**.

Please note that technical editing may introduce minor changes to the text and/or graphics, which may alter content. The journal's standard **Terms & Conditions** and the **Ethical guidelines** still apply. In no event shall the Royal Society of Chemistry be held responsible for any errors or omissions in this *Accepted Manuscript* or any consequences arising from the use of any information it contains.

# Titanium Functionalized α-Zirconium Phosphate Single Layer Nanosheets for Photocatalyst Applications

Yingjie Zhou,[1] Aoning Wang,[2] Zhoulu Wang,[2] Miao Chen,[2] Wei Wang,[1] Luyi Sun,[3] Xiang

Liu[2*]

[1]School of Physics and Optoelectronic Engineering, Nanjing University of Information

Science & Technology, 219 Ningliu Road, Nanjing, Jiangsu, 210044, China

[2] Key Laboratory of Flexible Electronics (KLOFE) & Institue of Advanced Materials

(IAM), National Jiangsu Synergistic Innovation Center for Advanced Materials (SICAM),

Nanjing Tech University (Nanjing Tech), 30 South Puzhu Road, Nanjing, Jiangsu,

211816, China

[3]Department of Chemical & Biomolecular Engineering and Polymer Program, Institute of

Materials Science, University of Connecticut, Storrs, Connecticut 06269, United States

*Authors to whom correspondence should be addressed:

Dr. Xiang Liu, Email: iamxliu@njtech.edu.cn

**ABSTRACT:**

Titanium species were immobilized on α-ZrP nanosheets (ZrP-Ti) by a modified post-grafting method. The obtained ZrP-Ti composites were characterized by Fourier transform infrared spectroscopy (FTIR), X-ray diffraction (XRD), X-ray photoelectron spectroscopy (XPS), transmission electron microscopy (TEM), ultraviolet-visible absorption spectroscopy (UV-vis), photoluminescence spectroscopy (PL), and scanning electron microscopy (SEM) techniques. The titanium species in the form of $TiO_{2-x}$ clusters with an average particle size of 2~5 nm were grafted on α-ZrP nanosheets via the chemical bonding with P elements. Such ZrP-Ti composites could be well dispersed in polar solvent to ensure that the $TiO_{2-x}$ clusters bonded on both faces of the nanosheets were accessible. The ZrP-Ti composites presented enhanced visible-light absorption properties compared with that of pure $TiO_2$. These features allowed them exhibit better photocatalytic activities for the photodegradation of methylene blue (MB) under solar irradiation. The $TiO_{2-x}$ clusters tend to aggregate to anatase phase $TiO_2$ when the molar ratio of P/Ti exceeded 1/1, however, this did reversely advantage in their photocatalytic activities. The best MB degradation efficiency of 100% with the apparent rate constant of 0.054 min$^{-1}$ could be achieved over the ZrP-Ti composite with the P/Ti molar ratio of 1/1.

2

## 1. INTRODUCTION

Heterogeneous photocatalysis as an advanced oxidation process has been the subject of a lot of studies related to air cleaning and water purification, because it offers the possibility of completely decomposing toxic chemicals.[1] Nanocrystalline titanium dioxide ($TiO_2$) has been recognized as one of the most promising photocatalyst among the numerous semiconductors due to its high oxidative power, low cost, nontoxicity, anticorrosion, and excellent stability.[2] However, the effective commercial applications are still challenged by two critical drawbacks.[3] The first one is the agglomeration of ultrafine powders resulting an adverse effect on catalyst performance. The second is that the degradation of organic pollutants by $TiO_2$ is limited to UV irradiation (only ~6% of solar radiation) due to its intrinsic large band gap (3.2eV for anatase and 3,0 eV for the rutile phase).[4, 5]

Recently, various strategies have been employed to enhance the photocatalytic efficiency of $TiO_2$, including morphological modifications by increasing surface area and porosity, or chemical modifications by the doping, loading and sensitization of $TiO_2$.[6] The high specific surface areas and nanosized particles would be beneficial for the large number and density of redox reaction sites due to their quantum confinement effects.[7] Recently, the major approach applied to produce high surface area $TiO_2$ is to create mesoporous structures in $TiO_2$ materials.[8, 9] However, the properties of $TiO_2$ is strongly dependent on the synthetic methods,[10] which limits its wide application. On the other hand, the chemical modification could possibly alter its electronic structures, which will

shift the light absorption towards visible light and/or to increase the lifetime of the photoproduced electron-holes pairs.[1] Up to date, doping $TiO_2$ with metal,[11-15] non-metal,[16-22] or coupling with semiconductors such as carbonaceous materials,[23-26] CdS,[27-29] $Fe_2O_3$[30-32] and $WO_3$[33] have been widely investigated to extend the photoresponse range of $TiO_2$ matrix. Nevertheless, improved photocatalytic activity is still necessary. Therefore, the synthesis of $TiO_2$ with high specific surface areas, nanosized particles, and films on glasses or other supports, combining with the chemical modification will improve the photocatalytic efficiency of $TiO_2$ under visible light.

α-Zirconium phosphate (α-ZrP, $Zr(HPO_4)_2 \cdot H_2O$) as a two dimensional (2D) nanomaterial, its lateral dimension can be altered by tuning the synthetic conditions.[34] Moreover, the α-ZrP crystals could be easily exfoliated into single nanosheets,[35-37] and the surface hydroxyl groups are fully exposed. Hence, the α-ZrP nanosheets has a higher surface energy compared to conventional 2D materials, such as graphite and its derivatives.[38] The P-OH moiety on the single nanosheets with a high density (4.2 groups/nm$^2$) and activity[35, 39-41] allow α-ZrP potentially be used as carrier for functional groups with a high loading density via the cation exchange or post grafting with alkoxyl groups. Such functionalized nanosheets are expected to be uniformly dispersed in a wide range of desired solvents, and the anchored functional groups are readily accessible, thus leading to high performance during applications.[37] The versatile properties of α-ZrP have been well studied and it has been applied for various applications.[42, 43]

In this work, we developed a facial method to anchor titanium species on α-ZrP

nanosheets (ZrP-Ti) with a high loading density, and the titanium species in the form of

$TiO_{2-x}$ clusters were considered to be doped by the P element in α-ZrP. The obtained

ZrP-Ti composites were fully characterized and investigated as homo-like heterogeneous

photocatalyst for the degradation of methylene blue under visible-light irradiation.

## 2. EXPERIMENTAL

### 2.1 Materials

Zirconyl chloride octahydrate ($ZrOCl_2·8H_2O$, 98%), phosphoric acid (85%),

1-propylamine (98%), tetrabutyl titanate ($Ti(OBu)_4$) were bought from Aladdin and used

as received. Reagent-grade ethanol, hydrochloric acid (HCl, 37 wt%) and toluene were

obtained from common commercial sources and used as received.

### 2.2 Preparation of single layer ZrP nanosheets

The pristine α-ZrP were synthesized via a hydrothermal method according to the

previously described process.[34] Typically, 6.0 g of $ZrOCl_2·8H_2O$ and 60.0 mL of 6.0 M

$H_3PO_4$ was sealed in a Teflon-lined pressure vessel for 24 h at 200 °C. 0.10 g of the

prepared α-ZrP were dispersed in 6.7 mL water, followed by mixing with 3.3 mL of 0.10

M 1-propylamine in an ice bath. The mixture was vigorously stirred until it became

transparent. Then 3.3 mL of 0.10 M HCl were added to the above mixture to regenerate

the protonated α-ZrP single layer nanosheets.[42, 44, 45] A gelatinous precipitate of the α-ZrP

nanosheets was collected by centrifugation and washed with water to eliminate chloride

ions under vigorous stirring. The obtained α-ZrP nanosheets gel was then washed with ethanol and centrifuged to exchange the solvent from water to ethanol. Subsequently, the α-ZrP nanosheets gel in ethanol was treated by toluene based on the same procedures and the process was repeated 3 times. This eventually led to the formation of α-ZrP nanosheets in toluene with the assistance of ultrasonication.

*2.3 Immobilization of titanium on* α-ZrP nanosheets

The immobilization of titanium species on α-ZrP nanosheets were prepared via a modified post-grafting method.[37] In a typical procedure, Ti(OBu)$_4$ was slowly added to the α-ZrP nanosheets in toluene with the assistance of ultrasonication to form the suspension, followed by stirring at 90 °C for 24 h. A gel-like precipitate of the precursor could be collected via centrifugation, and it was further rinsed with toluene three times. The precursor was then vacuum dried and calcined at 400 °C for 2 h to obtain the final product ZrP-Ti. The ZrP-Ti with various P/Ti molar ratios (1:0.8, 1:1, 1:1.2, 1:1.4) were prepared, and they were denoted as ZrP-Ti-1-0.8, ZrP-Ti-1-1, ZrP-Ti-1-1.2, and ZrP-Ti-1-1.4, respectively. In addition, the pure TiO$_2$ and TiO$_2$-P (P/Ti=1:1) were synthesized for control experiments. The TiO$_2$-P were prepared by replacing α-ZrP by 1M H$_3$PO$_4$ in the above process. The pure TiO$_2$ were obtained by the completely hydrolysis of Ti(OBu)$_4$ in the mixture of water and ethanol. The final obtained white powder was calcined at 400 °C for 2 h.

*2.4 Characterizations*

Fourier transform infrared spectroscopy (FTIR) spectra of the samples were

6

acquired on an Nicolet NEXUS-670 FTIR spectrophotometer using KBr pellet samples, which were made by grinding spectroscopic grade KBr and 0.1 wt% of the sample together.

X-ray diffraction(XRD) were performed on Rigaku Smartlab TM 9KW between 5 to 50° with Cu Kα (λ=0.154059nm) at 40 kV and 100mA.

X-ray photoelectron spectroscopy (XPS) spectra were recorded on PHI 5000 VersaProbe photoelectron spectrometer with monochromatic Al Kα radiation operated at 150 W. The shift of the binding energy due to the surface electrostatic charging were corrected using the C*1s* as an internal standard at 284.6 eV.

The morphological properties of prepared samples were imaged by scanning electron microscope (SEM, JSM-6360LV) operated at 15 kV.

The transmission electron microscopy (TEM) were observed on HT7700 with an accelerating voltage of 200 kV. The particles were dispersed in the mixture of ethanol and water, followed by being deposited on a carbon-film supported copper grid and air dried prior the measurement.

Ultraviolet-visible (UV-vis) absorbance spectra were collected on Lambda 950 UV-vis-NIR spectrometer equipped with an attachment of integrating sphere. Fine $BaSO_4$ power was used for baseline calibration and the spectra were recorded at a range of 250-700 nm.

The photoluminescence (PL) spectra were recorded by Hitachi F-4600 FL fluorescence spectrophotometer at room temperature using Hg-Cd laser as an excitation

7

light source. The excitation wavelength is 300 nm.

*2.5 Photocatalytic measurement*

The photocatalytic activity of the catalysts was evaluated by the photodegradation of methylene blue (MB) and phenol as model reactions. Typically, 50 mg photocatalysts were dispersed in 50 mL organic pollutant solution (10 mg/L), and ultrasonically vibrated in dark for 1 h to achieve adsorption/desorption equilibrium of MB. Irradiation was performed under the simulated solar light provided by a 250 W Xe lamp. The suspension was subjected to the light under continues stirring, and the distance between the light and the sample is 20 cm. Once the light illumination began, 3.5 mL of each sample was withdrawn from the suspension solution at an interval of 10 min. After the catalysts were separated by a syringe filter (0.45μm), the relative concentration of the supernatant solution was determined by the UV-vis absorbance at 576 nm for MB and 280 nm for phenol, respectively.

## 3. RESULTS AND DISCUSSION

The FTIR spectra of Ti(OBu)$_4$ grafted on α-ZrP with various P to Ti ratios are displayed in Figure 1, and the spectrum of the pristine α-ZrP was taken as a reference. As it is shown in the FTIR spectrum of the pristine α-ZrP, the vibrations of the hydration water molecules between the α-ZrP layers are located at 3597 and 3517 cm$^{-1}$, and the symmetric and bending vibrations of –OH groups are centered at 3158 and 1617 cm$^{-1}$,

8

respectively. The peaks at 1048 and 1125 cm$^{-1}$ are account for the symmetric and asymmetric stretch of P-O in PO$_2$ groups, and the peaks centered at 953 and 1253 cm$^{-1}$ are attributed to the out-of-plan and in-plane vibrations of the P-OH groups,[46, 47] respectively. The vibration of Zr-O can be observed at 525 and 592 cm$^{-1}$.[48, 49] After the Ti(OBu)$_4$ was grafted on α-ZrP, the characteristic bands assigned to the hydration water and P-OH groups in the pristine α-ZrP disappeared, meanwhile, the vibration peaks attributed to P-O in PO$_2$ groups became broader. Moreover, no characteristic bands belonged to tetrabutyl moieties could be observed. This could be due to the completely condensation reaction between the surface P-OH groups and the tetrabutyl groups in Ti(OBu)$_4$.
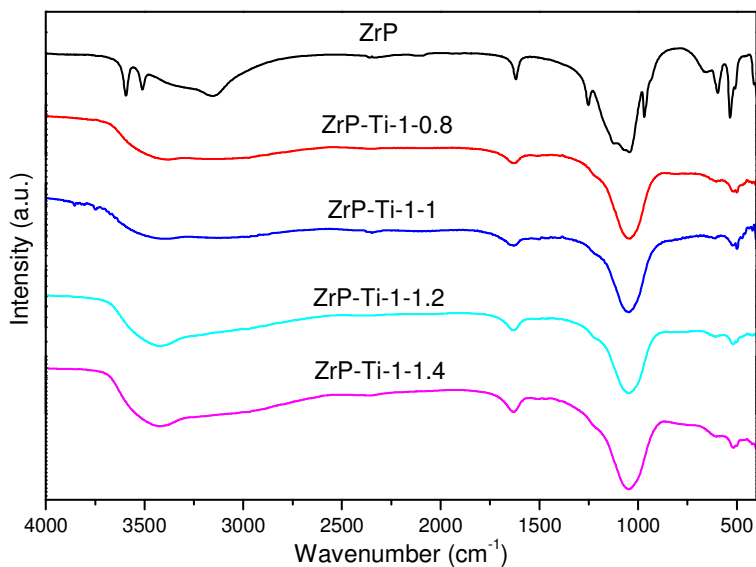


Figure 1. FTIR spectra of the pristine α-ZrP and Ti(OBu)$_4$ grafted on α-ZrP.

The XPS survey scan profiles of α-ZrP and the selected titanium species grafted on

α-ZrP (ZrP-Ti-1-1) are illustrated in Figure 2. The survey spectrum of ZrP-Ti-1-1 contains Ti *2p* peak in addition to the characteristic peaks of the pristine α-ZrP, confirming the attachment of Ti element on α-ZrP. As it is seen from the high-resolution scan of Ti *2p* region presented in Figure 3, the Ti $2p_{1/2}$ and Ti $2p_{3/2}$ spin-orbital splitting photoelectrons are located at binding energies of 464.6 eV and 458.5 eV, respectively. The binding energy of Ti *2p* shifted to a lower value of 0.10 eV compared with the reported literature value of bulk $TiO_2$ (458.4 eV),[50, 51] and this might be attributed to the quantum confinement effects caused by the $TiO_{2-x}$ clusters chemically bonded with the P element. The electronegative P will pull electrons in the Ti-O bond, which result in a little rise in the binding energy of Ti *2p*. To verify the chemical statues between the titanium species and P element in the α-ZrP nanosheets, the XPS spectra in the P*2p* and O *1s* range were recorded, and the results are displayed in Figure 4. The binding energies of P*2p* and O *1s* peaks of ZrP-Ti-1-1 shifts to a lower values in comparison to that of the pristine α-ZrP. These results support the reaction of the P-OH groups on the surface of α-ZrP nanosheets with the tetrabutyl groups of $Ti(OBu)_4$ to form the P-O-Ti bonds, suggesting that the titanium species are chemically bonded with P element, and this can also be verified by the FTIR characterization (Figure 1). The formation of P-O-Ti bond could be thought to be the replacement of Ti species by P species on the surface of the bulk $TiO_2$.[17] Therefore, the titanium species grafted on α-ZrP nanosheets could be thought to be in the form of P element doped $TiO_{2-x}$. However, as the ionic radius of Ti and P are not very similar to each other (0.067 and 0.038 nm, respectively), the mismatch would result

10

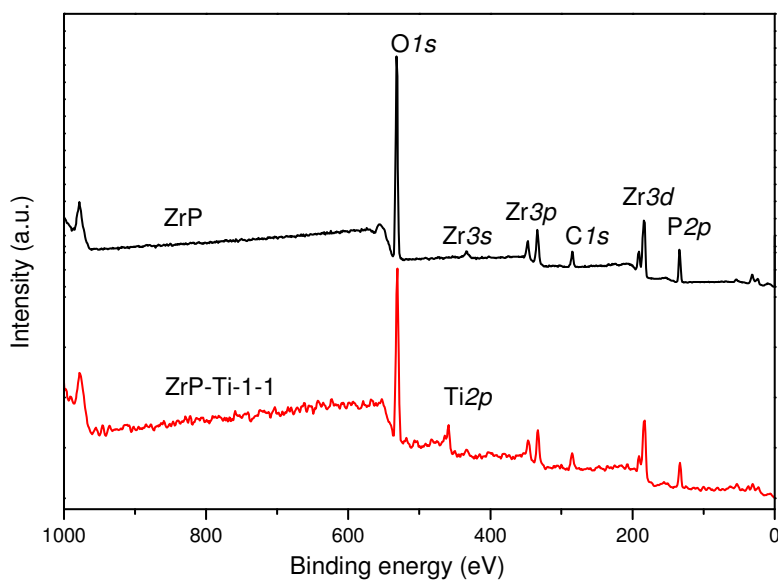numerous defects on the surface of the ZrP-Ti composites.



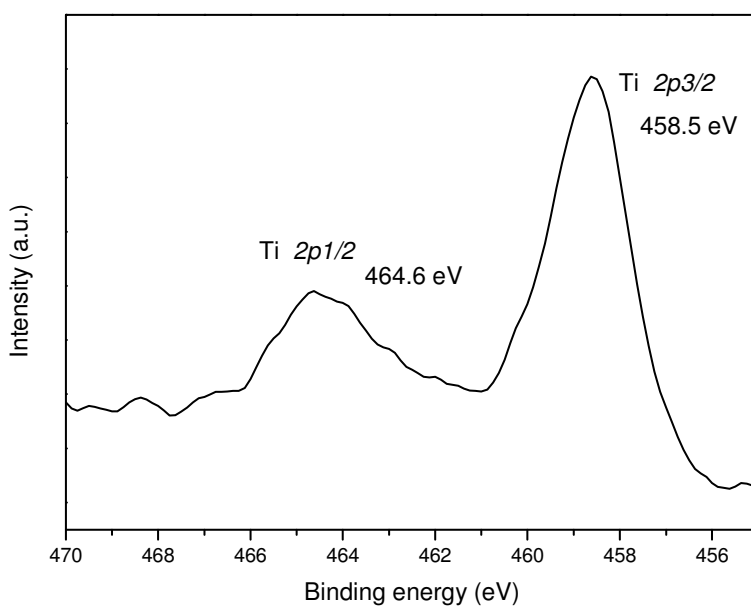Figure 2. The survey scan of the pristine α-ZrP and ZrP-Ti-1-1.



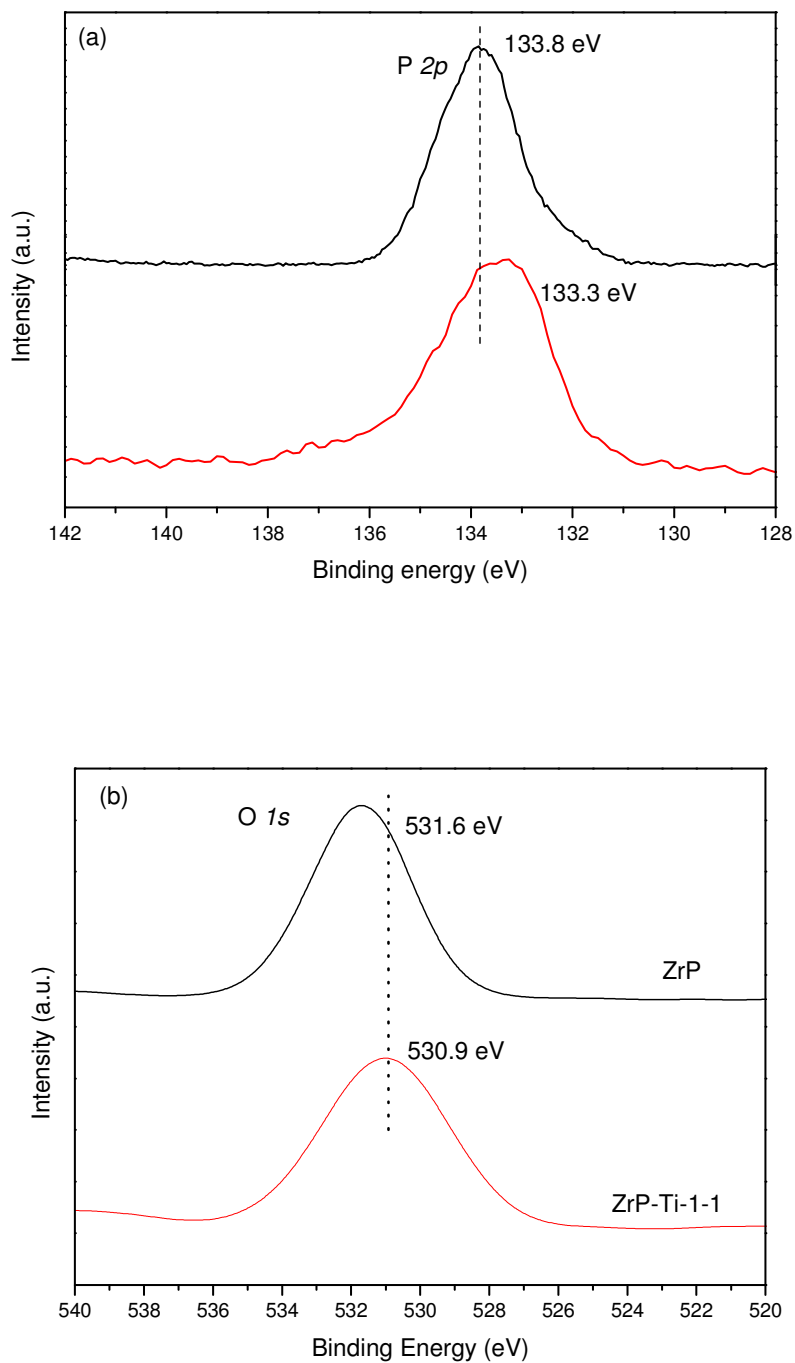Figure 3. High-resolution XPS scan of Ti *2p* of ZrP-Ti-1-1.

Figure 4. High-resolution XPS scan of (a) P *2p* and (b) O *1s*.

Figure 5 shows the XRD patterns of the pristine α-ZrP and the titanium species

modified α-ZrP. As it is shown in Figure 5, the pristine α-ZrP behaves a well crystalline

structure with an interlayer distance of 7.6 Å.[34-36] After the titanium species are grafted

onto the α-ZrP nanosheets surface, the crystallinity of the pristine α-ZrP disappeared and

a loosely layered structures with larger interlayer distances are formed.[37] As it is inferred

from the FTIR (Figure 1) and XPS (Figure 4) analysis, the quantum-sized $TiO_{2-x}$ clusters

are chemically bonded with P element on the α-ZrP nanosheets. The more Ti contents in

the ZrP-Ti composites, the larger the interlayer distance. The increased interlayer distance

is owing to the sandwiching of $TiO_{2-x}$ clusters between layers,[36] indicating that the $TiO_{2-x}$

clusters attached on the nanosheets act as a "spacer". Additionally, the $TiO_{2-x}$ clusters will

create the irregularities on the surface of the nanosheets, which are not favorable for the

re-stacking and thus leads to randomly arrangement of the individual nanosheet, and both

faces of the α-ZrP nanosheets are accessible in their applications. However, no diffraction

peaks belonged to $TiO_2$ could be observed when the molar ratio of P/Ti is less or equal to

1/1. This implies that the $TiO_{2-x}$ clusters with quantum sizes are mono-dispersed on the

individual α-ZrP nanosheet. When the molar ratio of P/Ti is above 1/1, the characteristic

diffraction peak at 2θ=38° assigned to the anatase type of $TiO_2$ could be observed,

suggesting that higher Ti contents in the ZrP-Ti composites will lead to the aggregates of

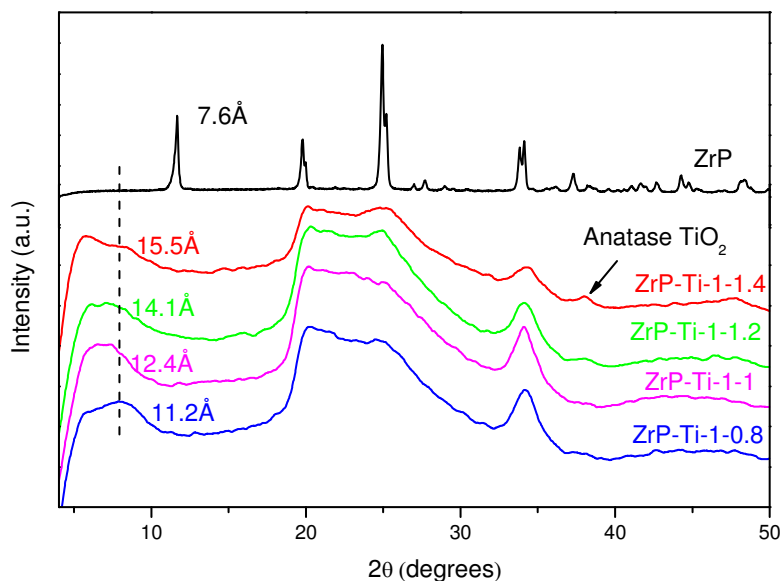$TiO_{2-x}$ into anatase phase $TiO_2$ with larger particle sizes.

Figure 5. XRD patterns of the pristine α-ZrP and titanium species modified α-ZrP.

The energy dispersive spectroscopy (EDS) analysis were performed to determine the exact molar ratios of P to Ti in the ZrP-Ti composites, and five parts of each sample are analyzed. The average data are shown in Table 1. The actual P/Ti molar ratios of the samples are slightly different from the nominal loading molar ratios in the synthetic process, this might be probably within the range of experimental error.

Table 1. EDS analysis of the Ti/P in the ZrP-Ti composites.

| Samples | P (At%) | Ti (At%) | Ti/P | P/Ti |
|---|---|---|---|---|
| ZrP-Ti-1-0.8 | 13.25 | 10.83 | 0.82 | 1.22 |
| ZrP-Ti-1-1 | 12.77 | 12.42 | 0.97 | 1.03 |
| ZrP-Ti-1-1.2 | 7.14 | 8.37 | 1.17 | 0.85 |

| ZrP-Ti-1-1.4 | 6.93 | 9.43 | 1.36 | 0.73 |
|---|---|---|---|---|

The surface morphology of α-ZrP and the ZrP-Ti nanocomposites were characterized by SEM and the results are presented in Figure 6. The pristine α-ZrP exhibits hexagonal shaped plates, suggesting a high crystallinity. After titanium species was grafted onto ZrP nanosheetsat different P/Ti formulating ratios, the shaped plates disappeared, and the nanosheets are tightly stacked, also a roughly layered morphology could be observed (Figure 6(b)-(e)). However, no obvious different observations can be seen for the ZrP-Ti nanocomposites with various P/Ti molar ratios.  To be noted, the morphologies of ZrP-Ti presented here are not the same as that of ZrP-Ti nanocomposites in suspension. Nonetheless, the particle sizes of $TiO_{2-x}$ clusters are still too small to be visualized directly from the SEM (Figure 6(b)-(f)) images. Overall, these results are highly consistent with the XRD analysis (Figure 5).
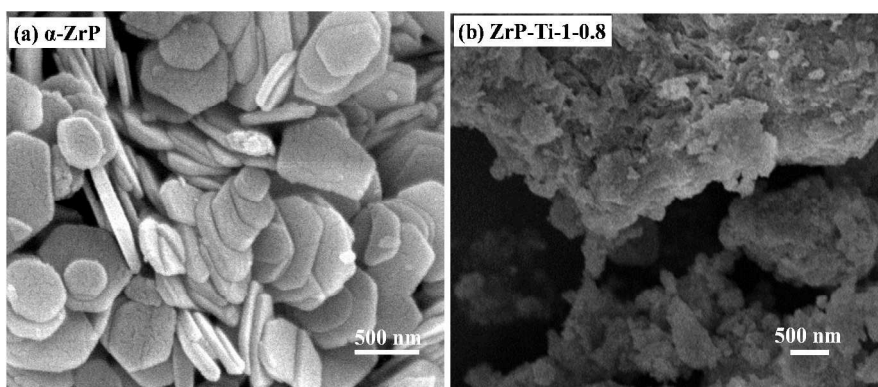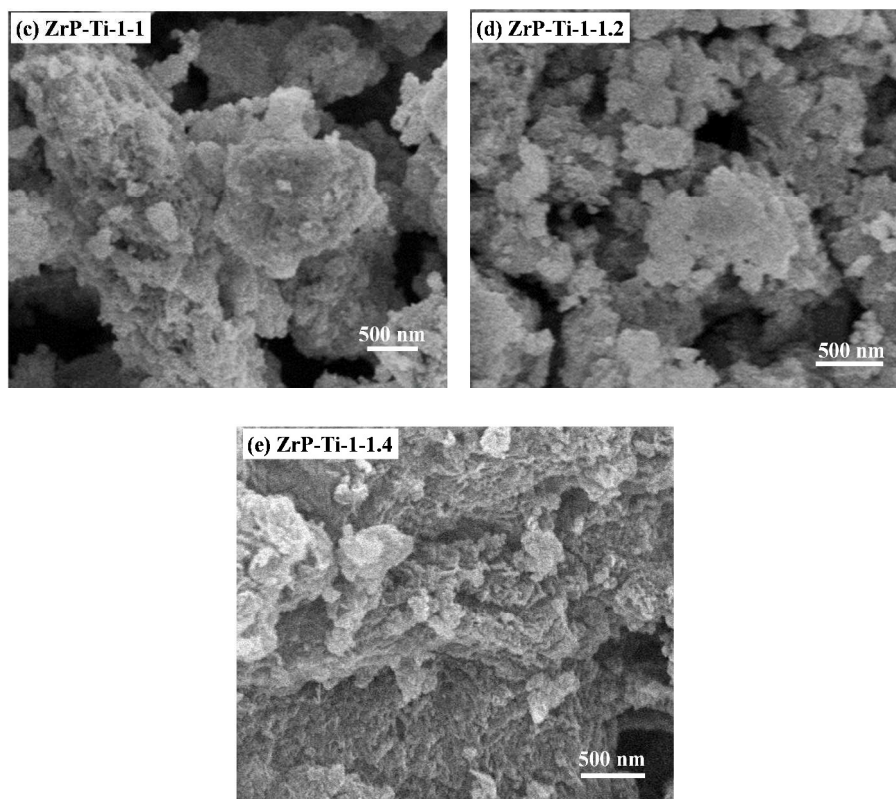
Figure 6. SEM images of (a) the pristine α-ZrP and (b)-(e) ZrP-Ti nanocomposites with various P/Ti molar ratios.

The pristine α-ZrP were exfoliated by 1-propylamine via ultrasonic vibration to produce α-ZrP nanosheets. TEM analysis were performed on the as-prepared α-ZrP nanosheets and ZrP-Ti-1-1, and the observations are shown in Figure 7. Figure 7(a) shows a general view of the exfoliated α-ZrP, clearly illustrating that the crystalline α-ZrP could be fully exfoliated to individual nanosheet by the process employed here. From the TEM of the ZrP-Ti presented in Figure 7((b)-(e)), it can be seen that all the transparent α-ZrP nanosheets are uniformly decorated by the $TiO_{2-x}$ clusters with particle size of around ca. 2~5 nm at higher P/Ti molar ratios, suggesting the stable mono-immobilization of quantum-sized $TiO_{2-x}$ clusters on the individual nanosheet when

the amount of titanium species is low. However, the $TiO_{2-x}$ clusters tend to aggregate into larger particles as the Ti concentration increases. These α-ZrP nanosheets possess large surface areas, and the $TiO_{2-x}$ clusters could be deposited on both sides of these nanosheets.[37] To be noted, these samples were ultrasonically dispersed in ethanol and a few drops were coated on carbon-film supported copper grids for TEM characterizations. Based on these information, it could be concluded that the ZrP-Ti composites could be well dispersed into polar solvents or reactants (such as $H_2O$, etc.), enabling the $TiO_{2-x}$ clusters to be highly accessible. Highly dispersed functional groups on supports with large surface areas have advantages in their applications, such as catalysis and sensors.[37, 52] Therefore, the ZrP-Ti composites synthesized here should be an effective potential photocatalyst, which will be discussed below.
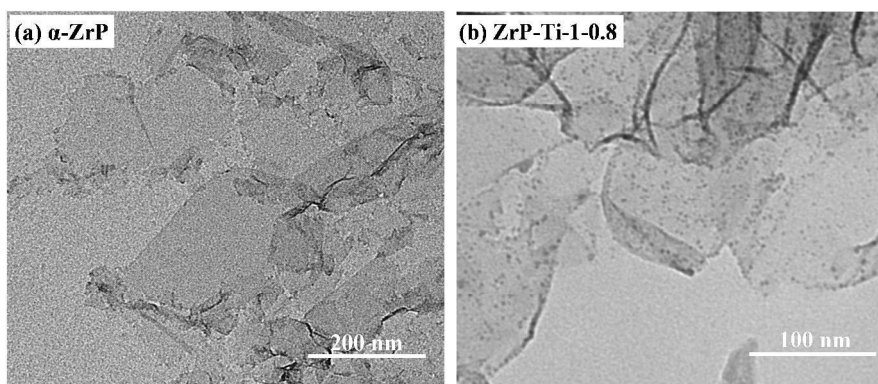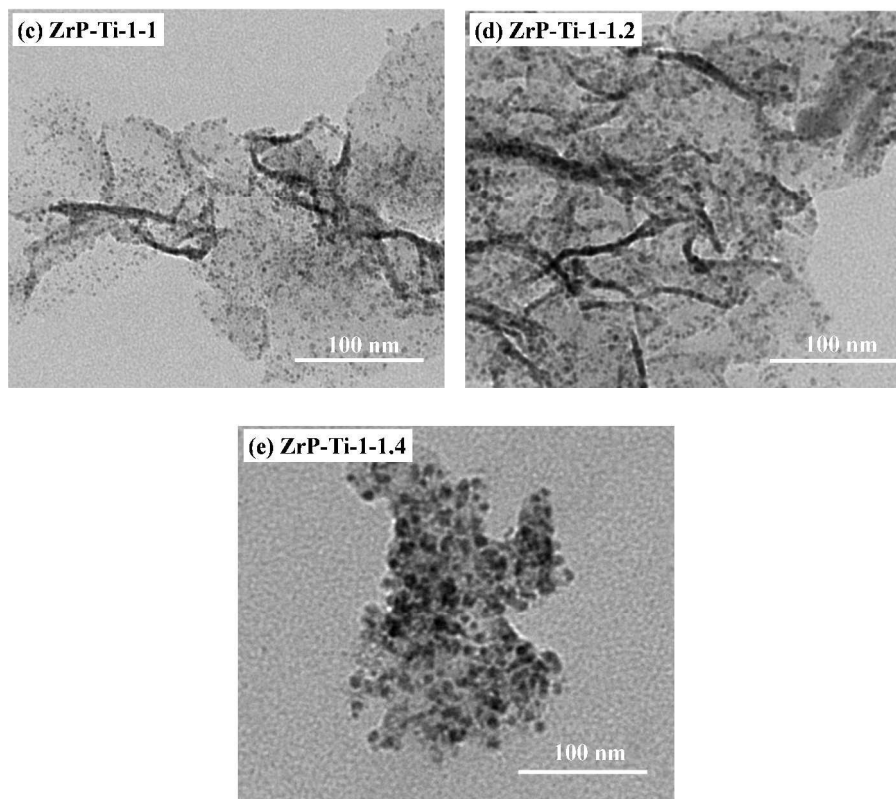
Figure 7. TEM images of (a) exfoliated α-ZrP and (b)-(e) ZrP-Ti nanocomposites with various P/Ti molar ratios.

Photoluminescence (PL) is a highly sensitive and powerful tool used to supply electronic and structural information for semiconductor materials, such as surface oxygen vacancies and defects, as well as the efficiency of charge carrier trapping, immigration and recombination.[15, 24, 53, 54] Figure 8 represents the room temperature PL spectra of pure $TiO_2$ and the ZrP-Ti compounds powders using Hg-Cd laser of 300 nm as excitation source. The photoluminescence features of $TiO_2$ are mainly originating from the self-trapped excitons, oxygen vacancies and surface states (defects).[15] PL spectrum of pure $TiO_2$ shows the clear emission bands at around 421 nm, 454 nm, 472 nm, and 486 nm, attributing to the radiative self-trapped excitons of anatase phase, surface traps,

oxygen vacancies, and the charge transfer transition from $Ti^{3+}$ to oxygen anion in a $[TiO_6]^{8-}$complex associated with surface oxygen vacancies,[15, 53, 55] respectively. However, the characteristic PL peak related to self-trapped excitons shifts to a lower wavelength at around 373 nm for all ZrP-Ti compounds. It may be due to the quantum confinement effect caused by the tinny $TiO_{2-x}$ clusters bonded with P elements on α-ZrP nanosheets. In addition, the characteristic PL peak positions in the visible-light range maintain the same as the pure $TiO_2$, but the overall PL intensities increase. The increased intensity can be ascribed to the high concentration of the surface defects in P doped $TiO_{2-x}$ moieties on α-ZrP nanosheets. This is because the surface defects provide good chances to bind electrons to form excitons. Thus, the exciton energy level near the bottom of the conduction band comes into being, and the PL band of the excitons can also occur.[56-58] The more surface defects, the higher concentration of the excitons. The observed PL intensity trend for the ZrP-Ti compounds in the visible region is ZrP-Ti-1-1<ZrP-Ti-1-1.2<ZrP-Ti-1-0.8<Zr-Ti-1-1.4. Moreover, The PL spectrum is the outcome of recombination of photogenerated electrons and holes, the lower PL intensity may indicate the lower radiative recombination rate of electrons and holes.[56] In summary, the PL intensities are the synergetic results of the electron-hole recombination rate, and the concentrations of the excitons. Based on these observations, it is expected that the ZrP-Ti-1-1 should have higher photocatalytic efficiency than other ZrP-Ti composites, because the catalytic activity of $TiO_2$ is proportional to the amount of excitons to be used in their respective redox reactions and inversely proportional to the photoinduced
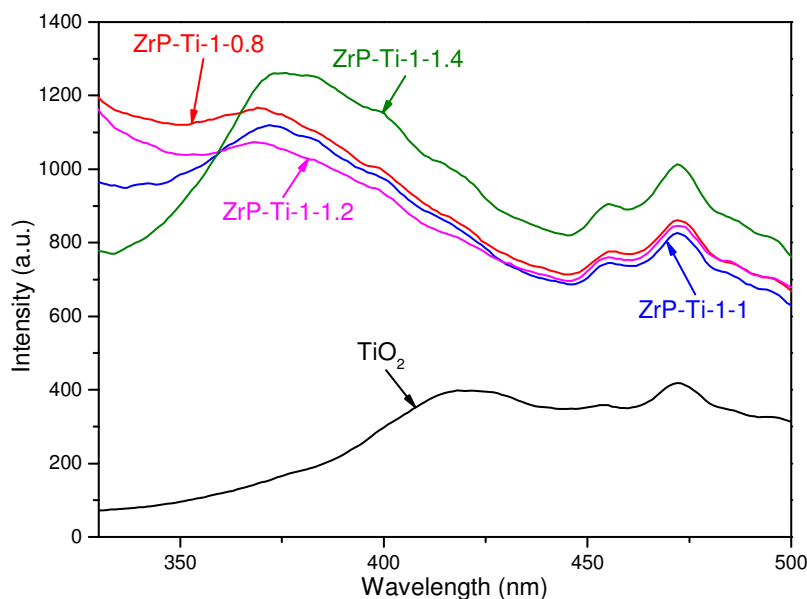
19

electron-hole recombination rate.[53]



Figure 8. Photoluminescence spectra of ZrP-Ti compounds with different Ti contents and inset represents the PL spectrum of pure $TiO_2$.

The UV-visible absorption spectra of the pristine α-ZrP, anatase phase $TiO_2$ and the ZrP-Ti composites are displayed in Figure 9. The pristine α-ZrP barely has no optical absorption. The pure $TiO_2$ reveals an intense absorption edge of approximately 400 nm. This could be assigned to the electronic transitions from the valance band to the conduction band for anatase phase according to its intrinsic band gap.[59, 60] The observed optical properties of ZrP-Ti composites are mainly attributed to the quantum size $TiO_{2-x}$ clusters bonded with P elements. All ZrP-Ti composites clearly exhibit a blue-shifted onset and broad absorption in the visible region as compared to the pure $TiO_2$, which

20

could be ascribed to the quantum confinement effect.[15, 61, 62] On the other hand, the light

absorption of the ZrP-Ti composites extend to the visible-light region, and this may be

attributed to the P element doping effect in the $TiO_{2-x}$ clusters.[63] In addition, the

absorption intensity in the visible-light range first increased and then decreased with

increasing Ti contents, and the ZrP-Ti-1-1 possesses the highest UV-vis absorption edge

and the highest visible-light absorption intensity.

The indirect band gap ($E_g$) values for pure $TiO_2$ and ZrP-Ti composites are estimated

by the Tauc equation ($\alpha h\nu = A(h\nu - E_g)^2$) using the UV-vis absorption data,[64-66] and the Tauc

plot is illustrated in Figure 10. By extrapolating the linear portion of the $(\alpha h\nu)^{1/2}$ versus h$\nu$

curves to the X-axis, the $E_g$ values could be obtained. The estimated indirect $E_g$ values for

pure $TiO_2$ is 2.90 eV, corresponding to the pure anatase phase bulk $TiO_2$.[15] The $TiO_2$-P

shows the highest band gap (3.1 eV). For the ZrP-Ti nanocomposites, the indirect $E_g$

values first decreased and then increased with the Ti contents, and the ZrP-Ti-1-1 shows

the lowest $E_g$ (2.6 eV). These results suggest that the titanium species immobilized on

α-ZrP nanosheets will decrease the $E_g$ of bulk $TiO_2$, and this is benefit for their

visible-light absorption. It is known that the light absorption in solids are related to their

electronic structures, which vary depending upon some factors like particle size, oxygen

deficiency, defects in materials, and so on.[5, 64, 67] The $TiO_2$ with a large quantity of surface

oxygen vacancies and defects can adsorb visible light,[5, 68-70] and the absorption intensities

are corresponding to the electron-hole separation efficiency,[4] which could be significantly

enhanced by decreasing the relative concentration ratio of bulk defects to surface defects

in $TiO_2$.[71, 72] In the synthesized ZrP-Ti composites, the $TiO_{2-x}$ moieties bonded with P element are the major source of active species for the visible-light absorption. Higher Ti contents in the ZrP-Ti composites definitely gives higher concentration of $TiO_{2-x}$ moieties. The poor visible-light absorption properties for ZrP-Ti-1-0.8 might be attributed to the small amount of $TiO_{2-x}$ moieties on the α-ZrP nanosheets. According to the XRD analysis (Figure 5), the $TiO_{2-x}$ moieties tend to aggregate into larger $TiO_2$ nanoparticles as the molar ratio of P/Ti is greater than 1/1. This will cause an increase in the relative concentration ratio of bulk defects to surface defects in the $TiO_{2-x}$ moieties, which is not good for the separation efficiency of photogenerated electrons and holes,[71] thus leading to the degradation in its visible-light absorption performance. The ZrP-Ti-1-1 presents the best visible-light absorption properties, because it possesses a large amount of surface oxygen vacancies and defects, as well as the high electron-hole separation efficiency.
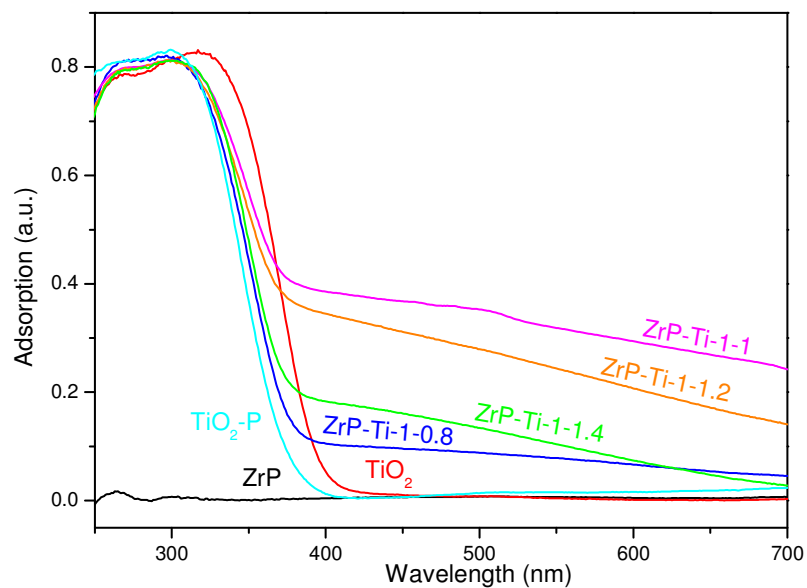
Figure 9. UV-visible absorption spectra of the pristine α-ZrP, anatase $TiO_2$ and the ZrP-Ti composites with various Ti contents.
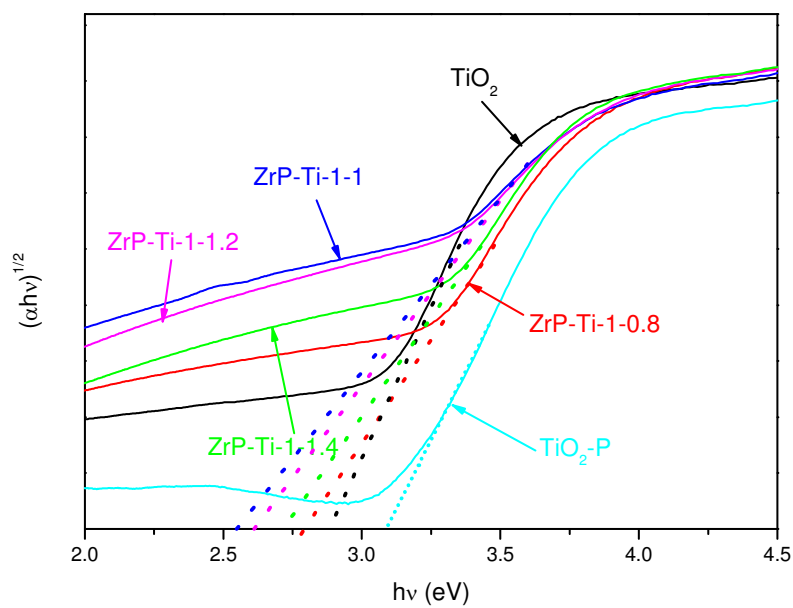


Figure 10. Optical band gap determination by Tauc plot of $TiO_2$, $TiO_2$-P and ZrP-Ti
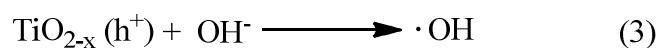
composites with various Ti contents.

In recent years, a considerable amount of dye-containing wastewater has been generated from textile, paper and printing industries, and this causes damage to the environment and dramatically threatens human health. The effective treatment of these wastewater is one of the most crucial problems before releasing them into the environment.[73] The photodegradation of dyes is the most hopeful resolution for wastewater purification, because it has the advantages of low cost, high efficiency and environment-friendly, but remains a great challenge.[74] The degradation of methylene blue (MB) under the irradiation of simulated solar light is selected as a model reaction to evaluate the photocatalytic activities of the synthesized photocatalysts. The pure $TiO_2$, $TiO_2$-P and the pristine α-ZrP are also evaluated for comparison under the same condition. Figure 11 shows the photocatalytic degradation of MB over different samples in the form of a plot of the relative concentration of MB ($C/C_0$) as a function of irradiation time. The slightly decrease in MB concentration (<1%) over the pristine α-ZrP is probably due to the physical adsorption of MB between the α-ZrP layers. The MB reduction over $TiO_2$ and $TiO_2$-P under light irradiation is much greater than the pristine α-ZrP, which clearly demonstrates that MB removal can be attributed to degradation rather than an absorption mechanism. However, the lower photocatalytic activity of $TiO_2$-P than $TiO_2$ is due to its worse UV-vis absorption property. In addition, it can be seen that all ZrP-Ti composites present higher photocatalytic activities for the decay of MB compared to pure $TiO_2$. The MB degradation efficiencies over the ZrP-Ti composites with various P/Ti molar ratios

24

are consistent with their visible-light absorption properties. That is, the degradation

efficiencies first increase and then decrease as the concentration of Ti is increased in the

ZrP-Ti composites. Particularly, the best degradation efficiency can reach 100% after 60

min periods for ZrP-Ti-1-1, which has the highest separation efficiency of the

photogenerated electron-hole pairs. The corresponding apparent rate constant $k$ could be

calculated according the following equation:[75-77] In $(C_0/C) = k$t, where $C_0$ is the initial

concentration of the pollutant after stirring in the dark for 1 h and $C$ is the residual

concentration of the organic pollutant measured after specified irradiation time, $t$. The

plot of In $(C_0/C)$ versus irradiation time and the slope of their linear regression ($k$) are

illustrated in Figure 12. Apparently, the degradation of MB follows the first order kinetics.

The pure $TiO_2$ presents the poorest $k$ of 0.005 $min^{-1}$. The value of $k$ for ZrP-Ti composites

first increases and then decreases with increasing Ti contents. The Zr-Ti-1-1 achieves the

highest $k$ of 0.054 $min^{-1}$, which matches the expectations from the optical properties.

Considering MB is a self-decomposing dye, the degradation of phenol[78] were

selected as another model reaction to better understand the photocatalytic activity of the

ZrP-Ti nanocomposites, and the photocatalytic results are presented in Figure 13. It is

seen that the ZrP-Ti-1-1 behaved the best phenol degradation efficiency of 62% in 70 min.

The degradation of phenol was found to be less as compared to the MB. But the

photocatalytic activities over the ZrP-Ti nanocomposites with various P/Ti molar ratios

showed the same trend as the photodegradation of MB.

The mechanism concerning the photodegradation of MB has been widely studied,[79]

the hydroxyl radicals ($\bullet$OH) play the major role for its oxidation and ring breaking to forming various byproducts such as carbon dioxide, water, nitrate, sulfate and hydrochloric acid compositions. Based on the characterizations of the ZrP-Ti nanocomposites, the $TiO_{2-x}$ is the major active component for the photocatalytic reaction. Thus, the mechanism of MB degradation over ZrP-Ti could be proposed as following equations (1), (2), (3). Firstly, the electrons and holes are generated in the ZrP-Ti under the simulated solar light irradiation. Then, the electron ($e^-$) in the conduction bands might be absorbed by dissolved oxygen to turn into a superoxide ($\bullet O_2^-$). Meanwhile, the hydroxyl radicals ($\bullet$OH) are generated by interaction of positive holes ($h^+$) in the valence bands with active OH groups in surface adsorbed water ($H_2O$). In the next step, the organic pollutants can be concurrently degraded during the photolysis process by interacting with the hydroxide radicals ($\bullet$OH) or superoxide ($\bullet O_2^-$).

$$TiO_{2-x} + h\nu \longrightarrow TiO_{2-x}\ (e^- + h^+) \quad (1)$$

$$TiO_{2-x}\ (e^-) + O_2 \longrightarrow \cdot O_2^- \quad (2)$$

$$TiO_{2-x}\ (h^+) + OH^- \longrightarrow \cdot OH \quad (3)$$

From the TEM analysis (Figure 7), the ZrP-Ti composites could be highly dispersed in the reaction system, and both faces of the α-ZrP nanosheets bonded with $TiO_{2-x}$ clusters are accessible in their applications. Thus, the improvement of the catalytic properties through ZrP-Ti composites is ascribed to the highly accessible $TiO_{2-x}$ clusters. In addition, the P doping is responsible for the visible-light absorption as indicated by the UV-vis results in Figure 9. As a result, a more utilization of the solar spectrum could be

achieved, which lead to higher photocatalytic activity. Higher visible-light absorption

definitely gives higher MB degradation efficiency. The ZrP-Ti composites are therefore
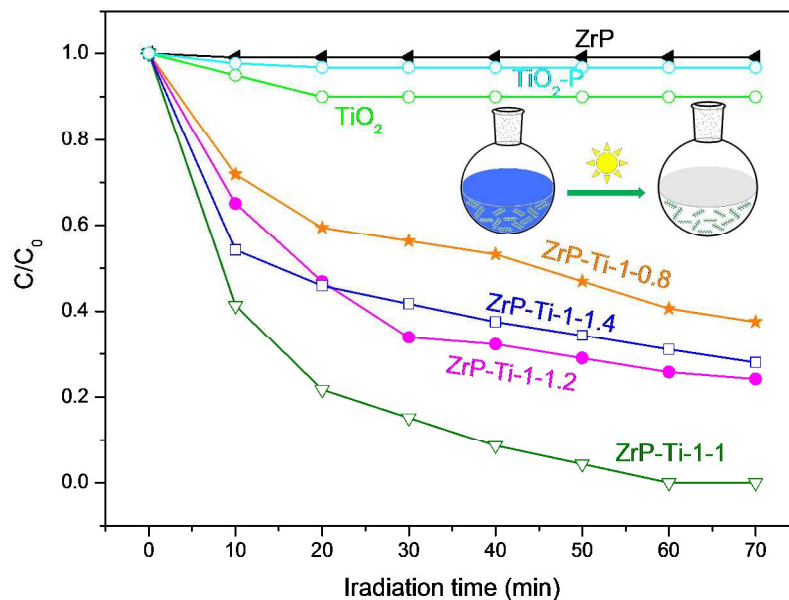
effective visible-light-driven photocatalysts.



Figure 11. MB degradation efficiency versus irradiation time (*t*) over different

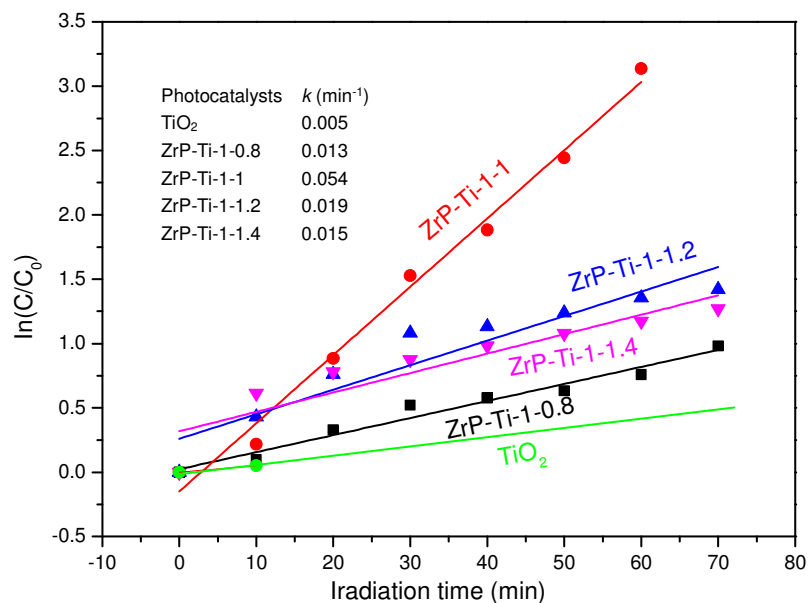photocatalysts under solar irradiation.

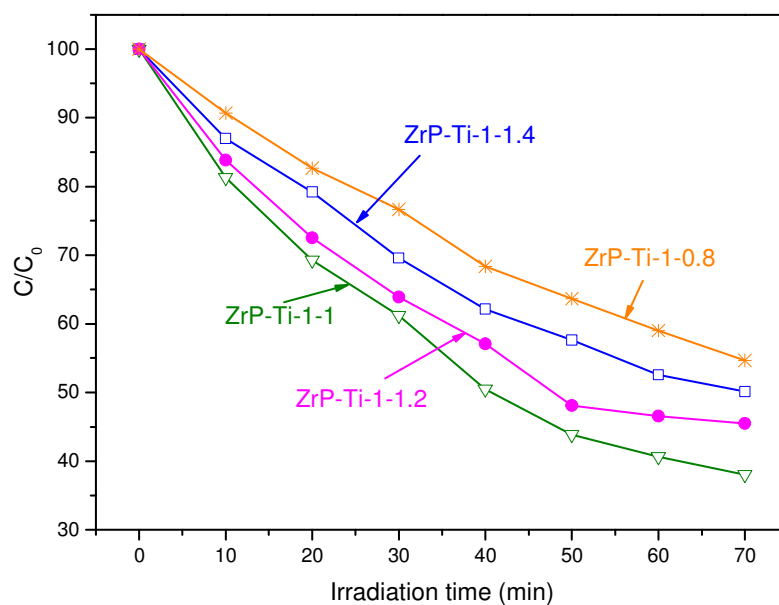Figure 12. The kinetics of MB photocatalytic degradation over different photocatalysts.



Figure 13. Phenol degradation efficiency versus irradiation time ($t$) over different photocatalysts under solar irradiation.

## 4. CONCLUSION

The titanium species immobilized on α-ZrP nanosheets (ZrP-Ti) were successfully prepared by a modified post-grafting method. The titanium species in the form of $TiO_{2-x}$ clusters were grafted on the nanosheets via the chemical bonding with P element in the α-ZrP. In other words, the P element doped $TiO_{2-x}$ clusters were mono-dispersed on α-ZrP nanosheets. These ZrP-Ti composites showed higher photocatalytic performance than that of pure $TiO_2$, and this was demonstrated by the photodegradation of MB under visible-light irradiation. The improvement was attributed to the highly accessible $TiO_{2-x}$ clusters as well as the enhanced optical properties caused by the P doping effects. However, when the molar ratios of P/Ti exceed 1/1, the $TiO_{2-x}$ moieties would agglomerated into anatase phase $TiO_2$, which went against the separation efficiency of the photogenerated electron-holes, thus led to the compromise in their photocatalytic activities. The ZrP-Ti with the P/Ti molar ratio of 1/1 showed the best MB degradation efficiency of 100% with the apparent rate constant of 0.054 $min^{-1}$.

## ACKNOWLEDGEMENT

## REFERENCES

1. A. Di Paola, E. García-López, G. Marcì and L. Palmisano, *Journal of Hazardous*

*Materials*, 2012, **211–212**, 3-29.

2. T. L. Thompson and J. T. Yates Jr, *Chemical Reviews*, 2006, **106**, 4428-4453.

3. E. S. Aazam, *Journal of Industrial and Engineering Chemistry*, 2014, **20**, 4033-4038.

4. W. Zhu, X. Qiu, V. Iancu, X.-Q. Chen, H. Pan, W. Wang, N. M. Dimitrijevic, T. Rajh, H. M. Meyer III and M. P. Paranthaman, *Physical Review Letters*, 2009, **103**, 226401-226404.

5. S. G. Kumar and L. G. Devi, *The Journal of Physical Chemistry A*, 2011, **115**, 13211-13241.

6. M. Pelaez, N. T. Nolan, S. C. Pillai, M. K. Seery, P. Falaras, A. G. Kontos, P. S. M. Dunlop, J. W. J. Hamilton, J. A. Byrne, K. O'Shea, M. H. Entezari and D. D. Dionysiou, *Applied Catalysis B: Environmental*, 2012, **125**, 331-349.

7. J. B. Joo, Q. Zhang, M. Dahl, I. Lee, J. Goebl, F. Zaera and Y. Yin, *Energy and Environmental Science*, 2012, **5**, 6321-6327.

8. H. Li, Z. Bian, J. Zhu, D. Zhang, G. Li, Y. Huo, H. Li and Y. Lu, *Journal of the American Chemical Society*, 2007, **129**, 8406-8407.

9. M. Zukalová, A. Zukal, L. Kavan, M. K. Nazeeruddin, P. Liska and M. Grätzel, *Nano Letters*, 2005, **5**, 1789-1792.

10. F. He, J. Li, T. Li and G. Li, *Chemical Engineering Journal*, 2014, **237**, 312-321.

11. S. Jensen and D. S. Kilin, *Journal of Physics-Condensed Matter*, 2015, **27**,

12. B. Tahir, M. Tahir and N. S. Amin, *Applied Surface Science,* 2015, **338**, 1-14.

13. L. L. Tan, W. J. Ong, S. P. Chai and A. R. Mohamed, *Applied Catalysis B: Environmental*, 2015, **166**, 251-259.

14. X. Fan, J. Wan, E. Liu, L. Sun, Y. Hu, H. Li, X. Hu and J. Fan, *Ceramics International*, 2015, **41**, 5107-5116.

15. A. K. Tripathi, M. C. Mathpal, P. Kumar, M. K. Singh, M. A. G. Soler and A. Agarwal, *Journal of Alloys and Compounds*, 2015, **622**, 37-47.

16. D. Zhao, C. Chen, Y. Wang, H. Ji, W. Ma, L. Zang and J. Zhao, *The Journal of*
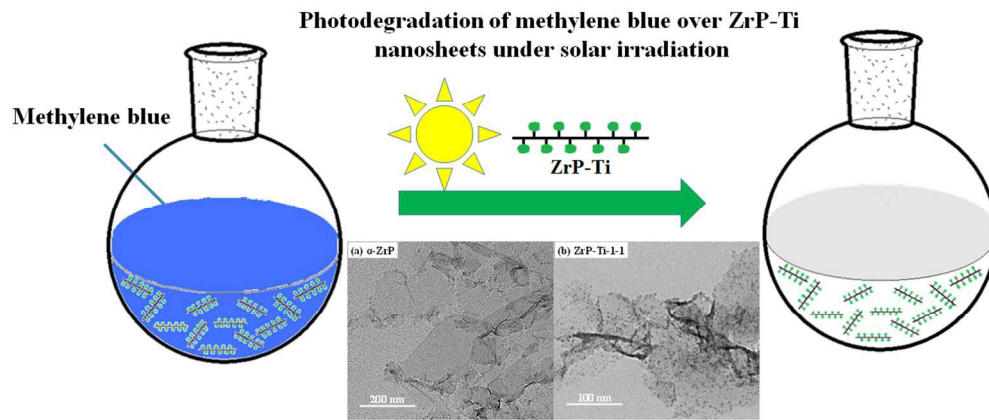
*Physical Chemistry C*, 2008, **112**, 5993-6001.

17. R. M. Mohamed and E. Aazam, *Chinese Journal of Catalysis*, 2013, **34**, 1267-1273.

18. M. Iwase, K. Yamada, T. Kurisaki, O. O. Prieto-Mahaney, B. Ohtani and H. Wakita, *Applied Catalysis B: Environmental*, 2013, **132**, 39-44.

19. S. K. Park, T. K. Yun and J. Y. Bae, *Journal of Nanoscience and Nanotechnology*, 2015, **15**, 5967-5970.

20. V. Vaiano, O. Sacco, D. Sannino and P. Ciambelli, *Applied Catalysis B: Environmental*, 2015, **170**, 153-161.

21. A. D. Mani, S. Muthusamy, S. Anandan and C. Subrahmanyam, *Journal of Experimental Nanoscience*, 2015, **10**, 115-125.

22. K. Yang, Y. Dai and B. Huang, *Journal of Physical Chemistry C*, 2007, **111**, 18985-18994.

23. X. L. Guo, J. Dai, K. Zhang, X. D. Wang, Z. Cui and J. Y. Xiang, *Textile Research Journal*, 2014, **84**, 1891-1900.

24. D. Y. Fu, G. Y. Han, F. F. Liu, Y. M. Xiao, H. F. Wang, R. Q. Liu and C. X. Liu, *Materials Science in Semiconductor Processing*, 2014, **27**, 966-974.

25. M. J. Sampaio, C. G. Silva, A. M. T. Silva, L. M. Pastrana-Martinez, C. Han, S. Morales-Torres, J. L. Figueiredo, D. D. Dionysiou and J. L. Faria, *Applied Catalysis B: Environmental*, 2015, **170**, 74-82.

26. R. Leary and A. Westwood, *Carbon*, 2011, **49**, 741-772.

27. S. K. Yadav and P. Jeevanandam, *Ceramics International*, 2015, **41**, 2160-2179.

28. Q. Li, B. Guo, J. Yu, J. Ran, B. Zhang, H. Yan and J. R. Gong, *Journal of the American Chemical Society*, 2011, **133**, 10878-10884.

29. L. Wu, J. C. Yu and X. Z. Fu, *Journal of Molecular Catalysis A: Chemical*, 2006, **244**, 25-32.

30. I. Jang, K. E. You, Y. C. Kim and S. G. Oh, *Applied Surface Science*, 2014, **316**, 187-193.

31. Z. Y. Han, Z. M. Du, Y. H. Zhang, L. S. Zhao and X. M. Cong, *Journal of Inorganic Materials*, 2014, **29**, 1110-1114.

32. R. van de Krol, Y. Liang and J. Schoonman, *Journal of Materials Chemistry*, 2008, **18**, 2311-2320.

33. S. Emin, M. de Respinis, M. Fanetti, W. Smith, M. Valant and B. Dam, *Applied Catalysis B: Environmental*, 2015, **166**, 406-412.

34. L. Sun, W. J. Boo, H.-J. Sue and A. Clearfield, *New Journal of Chemistry*, 2007, **31**, 39-43.

35. L. Y. Sun, W. J. Boo, R. L. Browning, H. J. Sue and A. Clearfield, *Chemistry of Materials*, 2005, **17**, 5606-5609.

36. L. Y. Sun, W. J. Boo, D. H. Sun, A. Clearfield and H. J. Sue, *Chemistry of Materials*, 2007, **19**, 1749-1754.

37. Y. Zhou, R. Huang, F. Ding, A. D. Brittain, J. Liu, M. Zhang, M. Xiao, Y. Meng and L. Sun, *ACS Applied Materials & Interfaces*, 2014, **6**, 7417-7425.

38. M. Xu, T. Liang, M. Shi and H. Chen, *Chemical Reviews*, 2013, **113**, 3766-3798.

39. M. Casciola, D. Capitani, A. Donnadio, G. Munari and M. Pica, *Inorganic Chemistry*, 2010, **49**, 3329-3336.

40. A. Diaz, B. M. Mosby, V. I. Bakhmutov, A. A. Marti, J. D. Batteas and A. Clearfield, *Chemistry of Materials*, 2013, **25**, 723-728.

41. B. M. Mosby, A. Diaz, V. Bakhmutov and A. Clearfield, *ACS Applied Materials & Interfaces*, 2014, **6**, 585-592.

42. L. Y. Sun, W. J. Boo, A. Clearfield, H. J. Sue and H. Q. Pham, *Journal of Membrane Science*, 2008, **318**, 129-136.

43. H. Hu, J. C. Martin, M. Xiao, C. S. Southworth, Y. Z. Meng and L. Y. Sun, *Journal of Physical Chemistry C*, 2011, **115**, 5509-5514.

44. W. J. Boo, L. Y. Sun, J. Liu, E. Moghbelli, A. Clearfield, H. J. Sue, H. Pham and N. Verghese, *Journal of Polymer Science Part B: Polymer Physics*, 2007, **45**, 1459-1469.

45. G. Alberti, M. Casciola, M. Pica and G. Di Cesare, *Annals of the New York Academy of Sciences*, 2003, **984**, 208-225.

46. S. E. Horsley, D. V. Nowell and D. T. Stewart, *Spectrochimica Acta Part A: Molecular Spectroscopy*, 1974, **30**, 535-541.

47. G. A. H. Mekhemer, *Colloids and Surfaces A: Physicochemical and Engineering Aspects*, 1998, **141**, 227-235.

48. C. G. Barraclough, D. C. Bradley, J. Lewis and I. M. Thomas, *Journal of the Chemical Society*, 1961, 2601-2605.

49. D. Das, N. Baliarsingh and K. Parida, *Journal of Molecular Catalysis A: Chemical*, 2007, **261**, 254-261.

50. B. Erdem, R. A. Hunsicker, G. W. Simmons, E. D. Sudol, V. L. Dimonie and M. S. El Aasser, *Langmuir*, 2001, **17**, 2664-2669.

51. S. Haukka, E. L. Lakomaa, O. Jylha, J. Vilhunen and S. Hornytzkyj, *Langmuir*, 1993, **9**, 3497-3506.

52. Y. Xing, *Journal of Physical Chemistry B*, 2004, **108**, 19255-19259.

53. H. Khan and D. Berk, *Journal of Photochemistry and Photobiology A: Chemistry*, 2014, **294**, 96-109.

54. C. Y. Jin, B. Liu, Z. X. Lei and J. M. Sun, *Nanoscale Research Letter*, 2015, **10**, 1-9

55. Y. Q. Kou, J. K. Yang, B. Li and S. C. Fu, *Materials Research Bulletin*, 2015, **63**, 105-111.

56. T. Toyoda, T. Hayakawa and Q. Shen, *Materials Science and Engineering: B*, 2000, **78**, 84-89.

57. Q. Y. Wang, H. Q. Jiang, S. Y. Zang, J. S. Li and Q. F. Wang, *Journal of Alloys and Compounds*, 2014, **586**, 411-419.

58. L. Jing, B. Xin, F. Yuan, L. Xue, B. Wang and H. Fu, *The Journal of Physical Chemistry B*, 2006, **110**, 17860-17865.

59. M. Iwase, K. Yamada, T. Kurisaki, B. Ohtani and H. Wakita, *Applied Catalysis*

*B-Environmental*, 2013, **140**, 327-332.

60. Z. Luo, A. S. Poyraz, C. H. Kuo, R. Miao, Y. T. Meng, S. Y. Chen, T. Jiang, C. Wenos and S. L. Suib, *Chemistry of Materials*, 2015, **27**, 6-17.

61. K. M. Reddy, S. V. Manorama and A. R. Reddy, *Materials Chemistry and Physics*, 2003, **78**, 239-245.

62. X. Xue, W. Ji, Z. Mao, H. Mao, Y. Wang, X. Wang, W. Ruan, B. Zhao and J. R. Lombardi, *The Journal of Physical Chemistry C*, 2012, **116**, 8792-8797.

63. Y. Xia, Y. S. Jiang, F. F. Li, M. S. Xia, B. Xue and Y. J. Li, *Applied Surface Science*, 2014, **289**, 306-315.

64. Alamgir, W. Khan, S. Ahmad, M. Mehedi Hassan and A. H. Naqvi, *Optical Materials*, 2014, **38**, 278-285.

65. J. Tauc, R. Grigorovici and A. Vancu, *Physica Status Solidi B*, 1966, **15**, 627-637.

66. N. Bayal and P. Jeevanandam, *Ceramics International*, 2014, **40**, 15463-15477.

67. T. N. Soitah, Y. Chunhui and S. Liang, *Science of Advanced Materials*, 2010, **2**, 534-538.

68. Z. Lin, A. Orlov, R. M. Lambert and M. C. Payne, *The Journal of Physical Chemistry B*, 2005, **109**, 20948-20952.

69. I. Nakamura, N. Negishi, S. Kutsuna, T. Ihara, S. Sugihara and K. Takeuchi, *Journal of Molecular Catalysis A: Chemical*, 2000, **161**, 205-212.

70. D. Li, H. Haneda, N. K. Labhsetwar, S. Hishita and N. Ohashi, *Chemical Physics Letters*, 2005, **401**, 579-584.

71. M. Kong, Y. Li, X. Chen, T. Tian, P. Fang, F. Zheng and X. Zhao, *Journal of the American Chemical Society*, 2011, **133**, 16414-16417.

72. D. Das and K. Parida, *Catalysis Surveys From Asia*, 2008, **12**, 203-213.

73. P. K. Malik, *Journal of Hazardous Materials*, 2004, **113**, 81-88.

74. B. Li and H. Cao, *Journal of Materials Chemistry*, 2011, **21**, 3346-3349.

75. J. Niu, B. Yao, Y. Chen, C. Peng, X. Yu, J. Zhang and G. Bai, *Applied Surface Science*,

2013, **271**, 39-44.

76. I. K. Konstantinou and T. A. Albanis, *Applied Catalysis B: Environmental*, 2004, **49**, 1-14.

77. Y. Liang, H. Wang, H. S. Casalongue, Z. Chen and H. Dai, *Nano Research*, 2010, **3**, 701-705.

78. D. P. Das, K. Parida and B. R. De, *Journal of Molecular Catalysis A: Chemical*, 2005, **240**, 1-6.

79. D. Das, N. Biswal, S. Martha and K. Parida, *Journal of Molecular Catalysis A: Chemical*, 2011, **349**, 36-41.

**Photodegradation of methylene blue over ZrP-Ti nanosheets under solar irradiation**

ZrP-Ti

Methylene blue

(a) α-ZrP

(b) ZrP-Ti-1-1

200 nm

100 nm

352x148mm (96 x 96 DPI)